

# Radiative trapping in intense laser beams

**J G Kirk**

Max-Planck-Institut für Kernphysik, Postfach 10 39 80, 69029 Heidelberg, Germany

E-mail: john.kirk@mpi-hd.mpg.de

**Abstract.** The dynamics of electrons in counter-propagating, circularly polarized laser beams are shown to exhibit attractors whose ability to trap particles depends on the ratio of the beam intensities and a single parameter describing radiation reaction. Analytical expressions are found for the underlying limit cycles and the parameter range in which they are stable. In high-intensity optical pulses, where radiation reaction strongly modifies the trajectories, the production of collimated gamma-rays and the initiation of non-linear cascades of electron-positron pairs can be optimized by a suitable choice of the intensity ratio.

PACS numbers: 12.20.-m, 52.27.Ep, 52.38.Ph

Journal reference: *Plasma Physics and Controlled Fusion* **8**, 085005 (2016)

## 1. Introduction

The design of experiments on 10 PW laser facilities that will probe strong-field QED [1, 2, 3] requires an understanding of the behaviour of electrons and positrons in intense photon beams [4]. However, in all but the simplest configurations, such as a single plane wave [5], the dynamics are highly complex, displaying regions of both ordered and chaotic motion [6, 7, 8]. Radiative reaction plays a crucial role at these intensities, and has been implemented in numerical studies by several groups, using both a classical and a fully quantum approach [9, 10, 11, 12, 13, 14, 15]. Amongst other effects, it leads to a contraction of phase-space, which can cause particle trajectories to accumulate on attractors [8, 16, 17, 18, 19]. This “radiative trapping” is an important effect, because it may allow the electrons and the gamma-rays they radiate to be controlled.

Attractors are closely related to limit cycles, which are periodic trajectories in phase space. When these are stable to infinitesimal perturbations, they correspond to a simple attractor, which confines trajectories that pass sufficiently close to the cycle. When they are unstable, an attractor with a more complicated structure (a strange attractor) may nevertheless be present in the immediate neighbourhood, and again lead to a concentration of particles in a restricted region of phase-space. The goal of this paper is to identify electron limit cycles analytically and to study their stability properties using both analytical and numerical tools. To achieve this, the treatment is restricted to classical electrodynamics. The chosen field configuration consists of two circularly

polarized, monochromatic, vacuum waves with arbitrary frequencies, amplitudes and propagation directions, but with opposite helicities. In classical electrodynamics, only two dimensionless parameters are needed to specify the relativistic dynamics in this set-up. These are the ratio  $\lambda$  of the wave amplitudes, and the classical radiation reaction parameter  $r_c$ , defined in equation (15). To date, work in this field has concentrated on numerical integration of trajectories in a standing wave, which corresponds to  $\lambda = 1$ . In this case, circularly polarized waves exhibit an attractor only where the electric field vanishes, and strong-field QED effects, such as the production of hard gamma-rays and electron positron pairs, are negligible.

In this paper, attractors are found on which the electric field amplitude and the particle energy are sufficient to permit strong-field QED effects in a limited range of  $\lambda$ . Expressions giving this range, the limit-cycle orbits and their linear stability properties as functions of  $\lambda$  and  $r_c$  are presented in section 3. Following this, numerical integration of the equations of motion is used in section 4 to present stroboscopic sections of phase-space illustrating the character of the particle orbits close to these limit cycles. The remainder of the paper is organized as follows: section 2 introduces the notation, presents the field configuration and formulates the equations of motion, section 5 relates the results to previous work and briefly discusses some practical implications, and section 6 summarizes the conclusions.

## 2. Field configuration and equations of motion

Consider two monochromatic plane waves in vacuum, with wave vectors  $\vec{k}_{1,2}/c$  and frequencies  $\omega_{1,2} = |\vec{k}_{1,2}|$ . Assuming  $\vec{k}_1 \neq \vec{k}_2$ , it is always possible to find a frame of reference in which these waves have the same frequency and oppositely directed wave vectors. In a system consisting of a single photon from wave 1, and a single photon from wave 2, this is the frame in which the total momentum is zero (the ZMF). In it, the waves have the frequency  $\omega = \left(\omega_1\omega_2 - \vec{k}_1 \cdot \vec{k}_2\right)^{1/2} / \sqrt{2}$ .

Our strategy is to look for limit cycles that lie entirely in the transverse plane, when viewed in the ZMF. On such orbits, the force exerted by the magnetic field must vanish. One obvious location is a plane in which the magnetic field itself vanishes, but this can occur only in very special configurations, such counter-propagating waves of equal amplitude and either aligned linear polarization or circular polarization of opposite helicity. More generally, one can search for orbits on which the particle velocity is always parallel to the magnetic field. Such orbits occur when the electric and magnetic field vectors corotate in the transverse plane such that their phase difference and amplitudes remain constant. In the remainder of this section, we show that this configuration is present in counter-propagating waves of arbitrary relative amplitude, provided they are of opposite helicity, and formulate the corresponding equations of motion.

The electric field is related to the dimensionless vector potential  $\vec{a}$  by  $\vec{E}_{1,2} = (mc/e) \partial \vec{a}_{1,2} / \partial t$ , where  $m$  and  $e$  are the mass and charge of the positron. For circularly

polarized waves, one can choose a Lorentz gauge in which  $|\vec{a}| = \text{constant}$  and the electrostatic potential vanishes. The ratio of the magnitudes of the dimensionless vector potentials can be defined as  $\lambda = a_2/a_1$ , where, without loss of generality,  $0 \leq \lambda \leq 1$ . Note that  $a_{1,2}$  and  $\lambda$  are Lorentz invariant, as is also the helicity of each wave. Thus, in terms of dimensionless independent variables ( $t \rightarrow t/\omega$ ,  $x \rightarrow xc/k$ ), the transverse components of the vector potentials in the ZMF can be written as

$$\begin{aligned}\mathbf{a}_1 &= \frac{a_0}{2} e^{\pm i(t-x+\phi_1)} \\ \mathbf{a}_2 &= \frac{\lambda a_0}{2} e^{\mp i(t+x+\phi_2)}.\end{aligned}\quad (1)$$

(Here, and in the following, the complex notation  $\mathbf{a} \equiv \vec{a} \cdot (\hat{y} + i\hat{z})$  is used for the transverse components of a vector.) In (1) the upper (lower) signs correspond to left-(right)-handed polarizations, the  $\phi_{1,2}$  are arbitrary phases, and the  $x$ -axis is chosen to lie in the direction of propagation of the primary wave (wave 1). The constant  $a_0$ , defined in equation (1) is the magnitude of the vector potential in the standing wave ( $\lambda = 1$ ), and will be used below to normalize the particle four-momentum. At fixed  $x$ , the amplitude of the superposed fields is constant in time, provided waves of opposite helicity are selected. Selecting convenient phases, and choosing left-handed polarization for wave 1, the vector potential is

$$\begin{aligned}\mathbf{a} &= \mathbf{a}_1 + \mathbf{a}_2 \\ &= ia_0 e^{it} (e^{-ix} + \lambda e^{ix})/2.\end{aligned}\quad (2)$$

Thus, in addition to the amplitudes, also the relative phase of the  $\vec{E}$  and  $\vec{B}$  vectors at a given location is constant in time:

$$\begin{aligned}|\vec{E}| &= \left(\frac{mc\omega}{e}\right) \frac{a_0}{2} [1 + \lambda^2 + 2\lambda \cos(2x)]^{1/2} \\ |\vec{B}| &= \left(\frac{mc\omega}{e}\right) \frac{a_0}{2} [1 + \lambda^2 - 2\lambda \cos(2x)]^{1/2} \\ \vec{E} \cdot \vec{B} &= \left(\frac{mc\omega}{e}\right)^2 a_0^2 \lambda \sin x \cos x.\end{aligned}\quad (3)$$

We now set  $m = c = 1$  and write the (dimensionless) four-momentum, as  $(\gamma, u_x, \mathbf{u}_\perp)$ , where  $\mathbf{u}_\perp = u_y + iu_z$  and  $\gamma = (1 + u_x^2 + \mathbf{u}_\perp \mathbf{u}_\perp^*)^{1/2}$ , and further introduce the canonical momentum in the transverse plane  $\mathbf{P}_\perp$  and its radial and angular components  $P_r$  and  $\Theta$  according to

$$\mathbf{P}_\perp \equiv sP_r e^{i\Theta} \quad (4)$$

$$= \mathbf{u}_\perp + s\mathbf{a}, \quad (5)$$

where  $s = q/e$ , with  $q$  the particle charge. In the absence of radiation reaction, the dynamics are Hamiltonian, with the three canonical momenta  $u_x$ ,  $P_r$  and  $\Theta$ . The

Hamiltonian function

$$\begin{aligned}
H(u_x, P_r, \Theta, x) &= \gamma \\
&= \left\{ 1 + u_x^2 + P_r^2 + \frac{a_0^2}{4} (1 + \lambda^2 + 2\lambda \cos 2x) \right. \\
&\quad \left. + a_0 P_r [\sin(t - \Theta - x) + \lambda \sin(t - \Theta + x)] \right\}^{1/2}
\end{aligned} \tag{6}$$

does not contain the coordinates conjugate to  $P_r$  and  $\Theta$ , indicating that these are constants of the motion. Ignoring the corresponding coordinates, the two remaining first-order equations of motion are

$$\frac{dx}{dt} = u_x/\gamma \tag{7}$$

$$\frac{du_x}{dt} = \frac{1}{\gamma} \left[ \lambda a_0^2 \sin x \cos x + \frac{a_0 P_r}{2} \cos(t - \Theta - x) - \frac{\lambda a_0 P_r}{2} \cos(t - \Theta + x) \right]. \tag{8}$$

Interestingly, the choice  $P_r = 0$  renders the Hamiltonian independent of time, so that the third constant of motion is  $\gamma$  and the system is integrable.

To take account of radiation reaction, we adopt the approximation used in [20], in which the spatial components of the four-force, are anti-parallel to those of the four-momentum. This approximation arises from the leading term in an expansion in  $1/\gamma$  of the radiation reaction force as formulated by [21] and is adequate to describe the orbits in large amplitude, circularly polarized waves. The radiation reaction terms are then

$$\left( \frac{d\vec{u}}{dt} \right)_{RR} = -\epsilon \left( \frac{mc^2}{\hbar\omega} \right)^2 \eta^2 \vec{u}/\gamma, \tag{9}$$

where

$$\epsilon = \frac{2e^2\omega}{3mc^3},$$

and  $\eta$  is the parameter that determines the importance of QED effects, defined in terms of the electromagnetic field tensor,  $F^{\mu\nu}$ , as

$$\eta = |F^{\mu\nu} u_\nu| / E_{\text{crit}}, \tag{10}$$

with  $E_{\text{crit}} = m^2 c^3 / e\hbar$  the critical or *Schwinger* field. Thus, retaining only the leading terms in  $1/\gamma$ , the equations of motion are

$$\frac{dx}{dt} = \hat{u}_x / \hat{\gamma} \tag{11}$$

$$\frac{d\hat{u}_x}{dt} = \frac{1}{2\hat{\gamma}} \left[ \lambda \sin 2x + \hat{P}_r \cos(t - \Theta - x) - \lambda \hat{P}_r \cos(t - \Theta + x) \right] - r_c \frac{\hat{\eta}^2 \hat{u}_x}{\hat{\gamma}} \tag{12}$$

$$\frac{d\hat{P}_r}{dt} = -r_c \frac{\hat{\eta}^2}{2\hat{\gamma}} \left[ 2\hat{P}_r + \sin(t - \Theta - x) + \lambda \sin(t - \Theta + x) \right] \tag{13}$$

$$\frac{d\Theta}{dt} = r_c \frac{\hat{\eta}^2}{2\hat{\gamma}\hat{P}_r} [\cos(t - \Theta - x) + \lambda \cos(t - \Theta + x)], \tag{14}$$

where we have introduced the classical radiation reaction parameter

$$r_c = \epsilon a_0^3 \quad (15)$$

[4, 22], and the four-momentum has been normalized to  $a_0$ :

$$\hat{u}_x = u_x/a_0 \quad (16)$$

$$\hat{P}_r = P_r/a_0 \quad (17)$$

$$\hat{\gamma} = \left\{ \hat{u}_x^2 + \hat{P}_r^2 + \frac{(1 + \lambda^2 + 2\lambda \cos 2x)}{4} + \hat{P}_r [\sin(t - \Theta - x) + \lambda \sin(t - \Theta + x)] \right\}^{1/2}. \quad (18)$$

For the transverse wave-fields given by equation (2),  $\eta$  can be written

$$\eta = \left( \frac{\hbar\omega}{mc^2} \right) a_0^2 \hat{\eta}, \quad (19)$$

where

$$\hat{\eta} \approx \frac{1}{2} \left\{ (1 + \lambda^2) (\hat{\gamma}^2 + \hat{u}_x^2) + 2\lambda \cos 2x (\hat{\gamma}^2 - \hat{u}_x^2) - 2(1 - \lambda^2) \hat{\gamma} \hat{u}_x - \lambda \left[ 2\hat{P}_r \cos(t - \Theta + x) - \sin 2x \right] \left[ 2\hat{P}_r \cos(t - \Theta - x) + \lambda \sin 2x \right] \right\}^{1/2}. \quad (20)$$

(The approximation made in equation (20) consists of making the replacement  $\gamma \rightarrow a_0 \hat{\gamma}$ .) Therefore, provided quantum effects are negligible and the motion is relativistic, the equations of motion (11–14) depend on only two parameters:  $\lambda$  and  $r_c$ .

### 3. Limit cycles and stability

Limit cycle solutions to the system (11–14) can be located by searching for points at which the parallel momentum  $\hat{u}_x$  vanishes (and, hence,  $x$  is constant), the azimuthal momentum  $\Theta$  is proportional to  $t$ , and the radial momenta  $\hat{P}_r$  is constant. Using the latter requirement, equation (13) determines  $\hat{P}_r$ . Substituting this expression into Eq (12), and setting  $\hat{u}_x = 0$  and  $\Theta = t + \theta_0$ , one finds that  $d\hat{u}_x/dt$  vanishes when

$$\theta_0 = \arctan \left( \frac{-(1 + \lambda) \tan x}{(1 - \lambda)} \right), \quad (21)$$

at which point

$$\hat{P}_r = -\frac{2\lambda\hat{\gamma}}{1 - \lambda^2} \sin(2x) \quad (22)$$

and

$$\hat{\eta} = \hat{\gamma}^2. \quad (23)$$

Finally, the self-consistency requirement  $d\Theta/dt = 1$ , determines the values of the initial phase  $\theta_0$ . If it can be fulfilled at a point  $x$ , limit cycles exist at  $x + n\pi$  for integer values

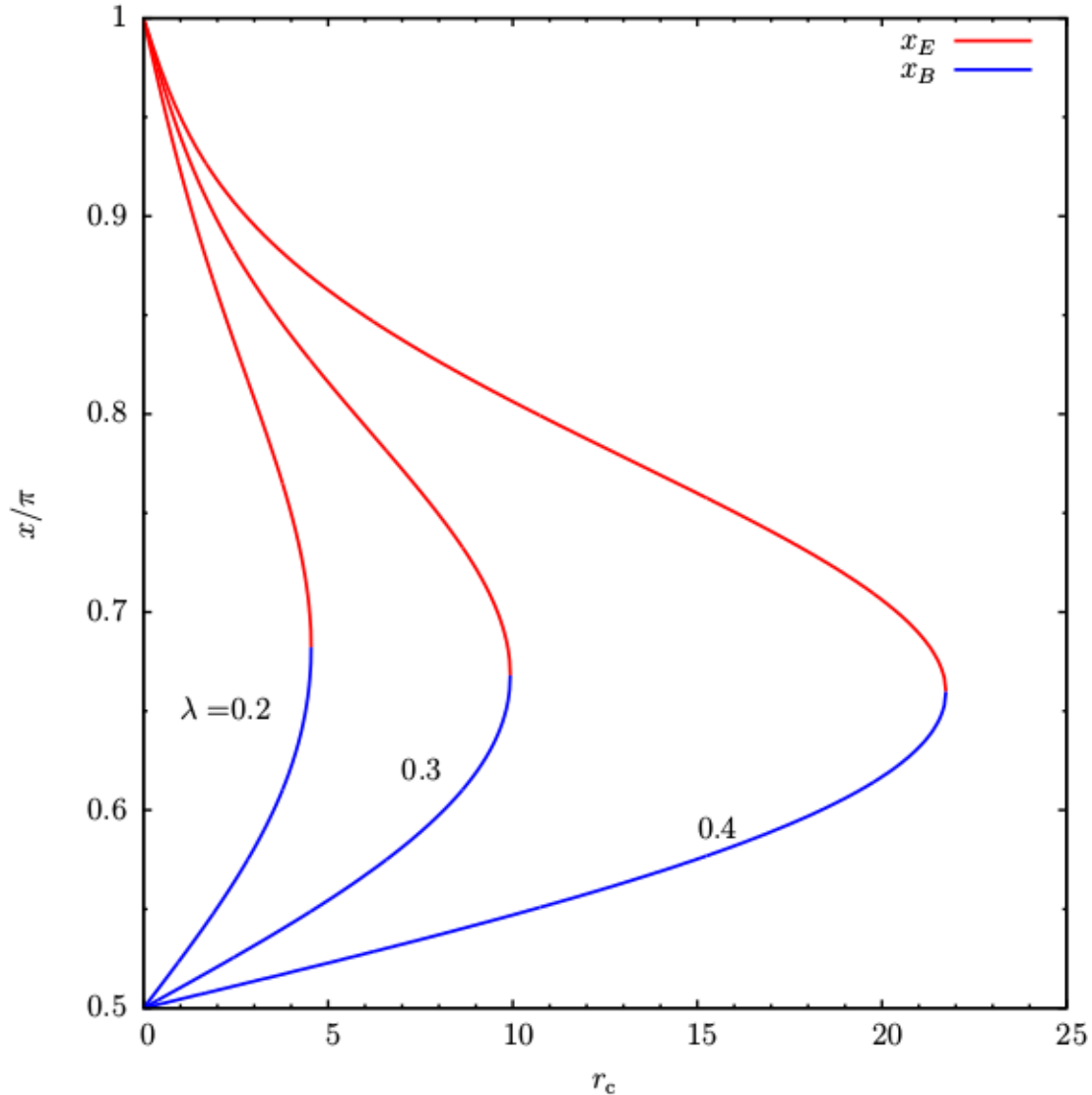


**Figure 1.** The location of the limit cycles as a function of the radiation reaction parameter  $r_c$  [see equation (15)] for three values of the ratio  $\lambda$  of the wave amplitudes. The suffix  $E$  ( $B$ ) denotes the cycle that is located close to the antinode of the electric (magnetic) field in the standing wave that exists when  $\lambda = 1$ .

of  $n$ , and consist of circular trajectories in the  $y$ - $z$  plane. The trajectories at even and odd values of  $n$  are essentially identical, i.e., particles rotate in the same sense but with a phase difference of  $\pi$ .

These points can be found by considering  $d\Theta/dt$  as a function of  $r_c$ ,  $\lambda$  and  $x$ , using (22) to substitute for  $\hat{P}_r$  and (21) to substitute for  $\theta_0$ . Then, for fixed  $\lambda$ , the function  $d\Theta/dt - 1$  has roots which coincide with those of a fifth order polynomial in  $\tan^2 x$ . For small  $r_c$ , there are two roots, which are conveniently chosen to lie in the range  $\pi/2 \leq x \leq \pi$ . As  $r_c$  increases the roots approach each other and vanish for  $r_c$  larger

than a critical value, given by:

$$r_{\max}(\lambda) = \frac{32\lambda}{(1-\lambda)^4} \left[ \frac{(8\lambda + \Delta)(1 + 6\lambda + \lambda^2 + \Delta)^3}{(1 + 10\lambda + \lambda^2 + \Delta)^5} \right]^{1/2}, \quad (24)$$

where

$$\Delta = \sqrt{1 + 62\lambda^2 + \lambda^4}.$$

For  $r_c \ll \lambda$ , the limit cycles lie close to  $\pi/2$  and  $\pi$ , and approximate expressions can be found. For the cycle that is close to  $x = \pi/2$  (which is an antinode of the magnetic field when  $\lambda = 1$ , hence the suffix  $B$ ) one has, to lowest order in  $r_c$  and for fixed  $\lambda$ :

$$x = x_B \approx \frac{\pi}{2} + \frac{r_c(1-\lambda)^4(1+\lambda)}{32\lambda} \quad (25)$$

$$\hat{P}_r \approx \frac{r_c(1-\lambda)^4}{16} \quad (26)$$

$$\Theta \approx t - \frac{\pi}{2} - \frac{r_c(1-\lambda)^5}{32\lambda} \quad (27)$$

$$\hat{\gamma} \approx \frac{1-\lambda}{2} \quad (28)$$

$$\hat{\eta} \approx \frac{(1-\lambda)^2}{4} \quad (29)$$

and for the cycle that is close to  $\pi$  (an antinode of the electric field when  $\lambda = 1$ ):

$$x = x_E \approx \pi - \frac{r_c(1-\lambda)(1+\lambda)^4}{32\lambda} \quad (30)$$

$$\hat{P}_r \approx \frac{r_c(1-\lambda)^4}{16} \quad (31)$$

$$\Theta \approx t + \pi + r_c \frac{(1+\lambda)^5}{32\lambda} \quad (32)$$

$$\hat{\gamma} \approx \frac{1+\lambda}{2} \quad (33)$$

$$\hat{\eta} \approx \frac{(1+\lambda)^2}{4}. \quad (34)$$

In the general case, a root-finding algorithm is necessary in order to locate  $x_E$  and  $x_B$ ; the results are shown in Fig 1.

It is easy to understand on physical grounds that such a limit cycle cannot exist for all values of  $\lambda$  and  $r_c$ . In a single, circularly polarized plane wave in the absence of radiation reaction, a circular trajectory that lies in the  $y$ - $z$  plane can always be found by choosing a suitable value of  $\hat{P}_r$ . However, the radiation reaction force acts to push the particle in the direction of propagation of the wave, eventually accelerating it to arbitrarily high energy [23]. On a limit cycle, this tendency must be opposed by a counter-propagating wave. Clearly, the stronger the radiation reaction, the higher must be the amplitude of the counter-propagating wave. Thus, for fixed  $\lambda$ , one expects limit

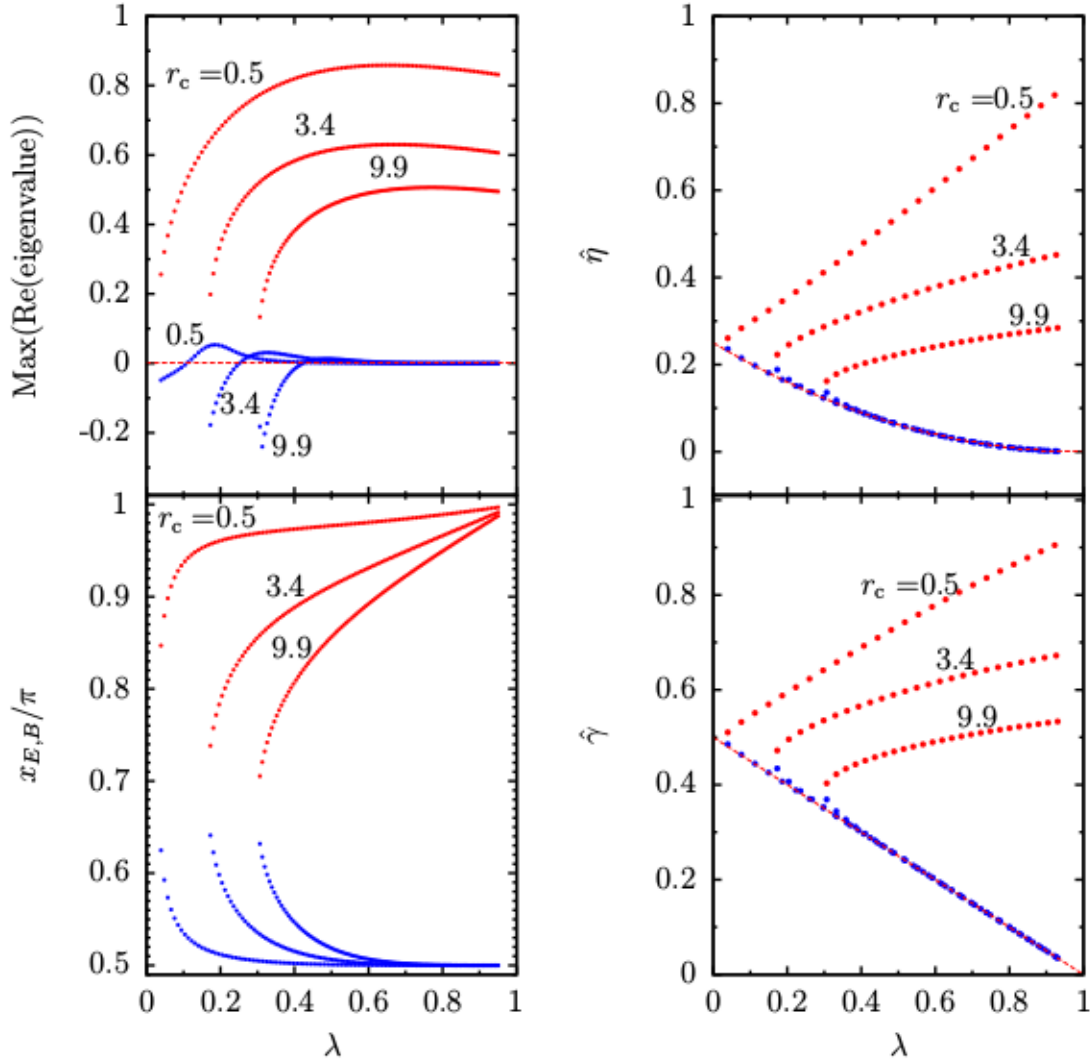


**Figure 2.** Properties of the limit cycles for three values of  $r_c$ . The cycles lie in the  $y$ - $z$  plane, at the location shown in the lower left panel. The top left panel shows the largest of the real parts of the eigenvalues of the Jacobian (35). Cycles located at  $x_E$ , plotted in red, are unstable for all  $r_c$ , those at  $x_B$ , shown in blue, have a region of stability below a critical value of  $\lambda$ , but are unstable above it. The cycles consist of circular motion at constant Lorentz factor, and constant value of the QED parameter  $\eta$ . The scaled values of these quantities  $\hat{\gamma}$  and  $\hat{\eta}$  [see equations (18) and (19)] are shown in the lower right and upper right panels, respectively, which also plot the approximations given by equations (28) and (29) as dashed, red lines.

cycles only for  $r_c$  less than some maximum value. As  $\lambda \rightarrow 1$ , i.e., in the standing wave,  $r_{\max} \rightarrow \infty$ , and the limit cycles approach  $\pi/2$  and  $\pi$ , which are the antinodes of  $\mathbf{B}$  and  $\mathbf{E}$ , and nodes of  $\mathbf{E}$  and  $\mathbf{B}$ , respectively. At fixed  $\lambda$ , figure 1 shows that the limit cycles are located at these same points when  $r_c \rightarrow 0$ . In this limit, particles extract no energy from the fields, implying that their velocity is perpendicular to the electric field. Although the fields do not have nodes when  $\lambda \neq 1$ , they are perpendicular to each other at  $x = \pi/2$  and  $x = \pi$ , as can be seen from Eq (3).

The importance of these limit cycles depends crucially on their stability. A linear analysis is straightforward to perform, because the Jacobian  $J$  of the system (11–14) is independent of time when evaluated on a limit cycle, where  $\Theta = t + \text{constant}$ . After some calculation, one finds that on such a cycle

$$\begin{aligned}
 J &= \begin{pmatrix} \partial\dot{x}/\partial x & \partial\dot{x}/\partial u_x & \partial\dot{x}/\partial P_r & \partial\dot{x}/\partial\Theta \\ \partial\dot{u}_x/\partial x & \dots & \dots & \dots \\ \partial\dot{P}_r/\partial x & \dots & \dots & \dots \\ \partial\dot{\Theta}/\partial x & \dots & \dots & \dots \end{pmatrix} \\
 &= \begin{pmatrix} 0 & \frac{1}{\hat{\gamma}} & 0 & 0 \\ \frac{\lambda \cos 2x - \hat{P}_r^2}{\hat{\gamma}} & -\frac{r_c \hat{\eta}^2}{\hat{\gamma}} & -\frac{\lambda \sin 2x}{2\hat{P}_r \hat{\gamma}} & 0 \\ -\frac{r_c \lambda \hat{\eta}^2 \sin 2x}{2\hat{P}_r \hat{\gamma}} & 0 & -\frac{r_c \hat{\eta}^2}{\hat{\gamma}} & \hat{P}_r \\ -\frac{\lambda \hat{\gamma}^2 \sin 2x}{\hat{\eta}^2} & -\frac{(1-\lambda^2)\hat{\gamma}}{2\hat{\eta}^2} & -\frac{\lambda^2 \sin^2 2\theta_0}{2\hat{\eta}^2 \hat{P}_r} - \frac{1}{\hat{P}_r} & \frac{[2\lambda r_c \hat{\eta}^2 \sin 2\theta_0 - \hat{\gamma}(1+\lambda^2+2\lambda \cos 2x)+2\hat{\eta}^2/\hat{\gamma}]\hat{P}_r^2}{2r_c \hat{\eta}^4} \\ & & & -\frac{r_c \hat{\eta}^2}{\hat{\gamma}} \end{pmatrix} \quad (35)
 \end{aligned}$$

Thus, the limit cycle is stable when the real part of each eigenvalue of (35) is negative, and unstable when the real part of any eigenvalue is positive.

As  $r_c \rightarrow 0$ , with  $\lambda$  held constant, one finds that the four eigenvalues  $s_E$  of the Jacobian of the limit cycle at  $x = x_E$  tend to the values

$$s_E \rightarrow \pm i(1 + \lambda)/2, \pm \sqrt{\lambda}, \quad (36)$$

showing that these cycles are unstable. On the other hand, on the limit cycle at  $x = x_B$ , they tend to purely imaginary values:

$$s_B \rightarrow \pm i(1 - \lambda)/2, \pm i\sqrt{\lambda}, \quad (37)$$

indicating marginal stability on the  $r_c = 0$  axis. The lowest order term in  $r_c$  in an

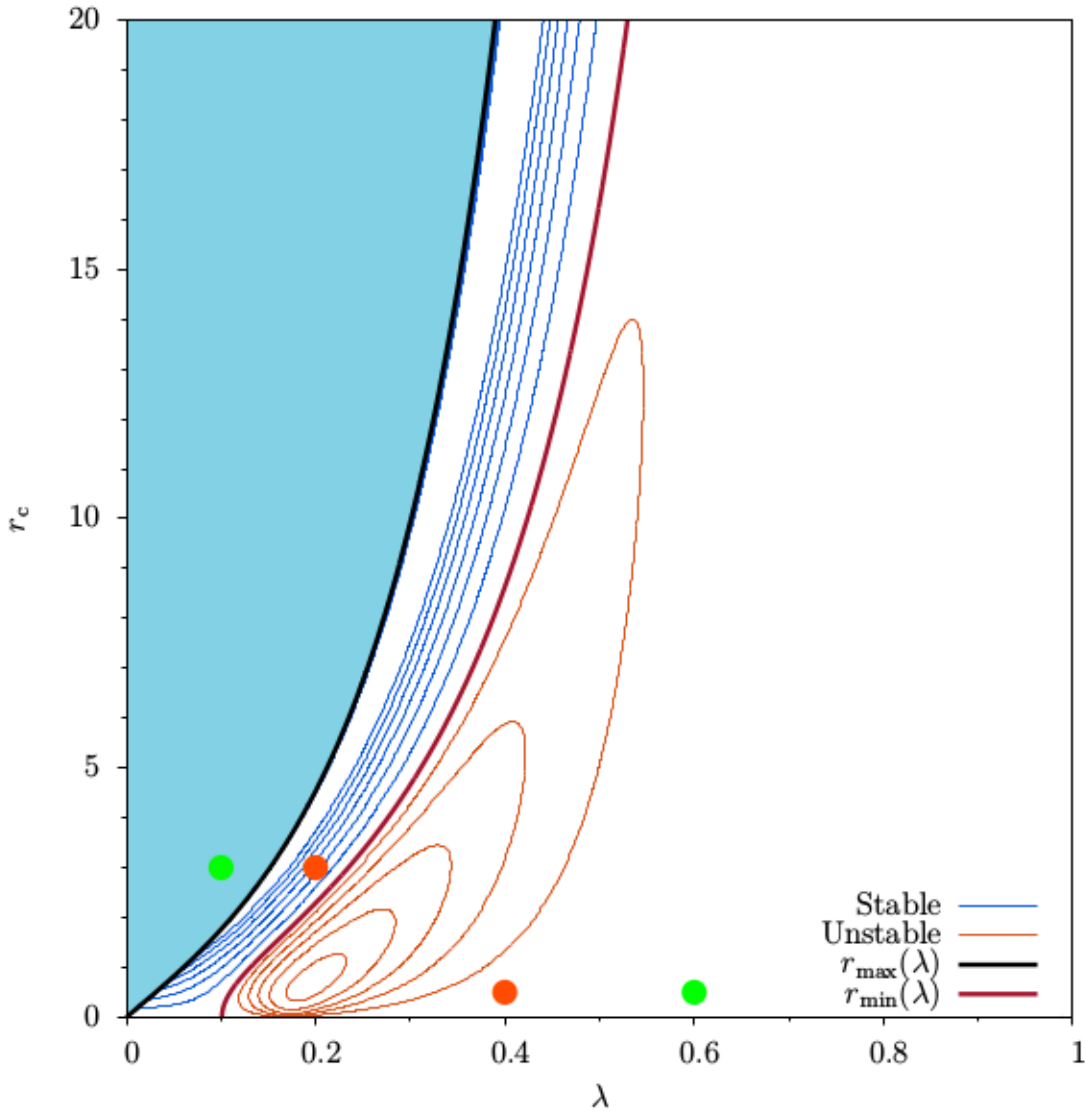


**Figure 3.** Contour plot of the largest real part of the eigenvalues of the Jacobian (35), evaluated on the limit cycle at the point  $x = x_B$ . Contours are equally spaced, between  $-0.02$  and  $-0.12$  in the stable region (blue), and between  $0.01$  and  $0.06$  in the unstable region (orange). Also plotted is the line of marginal stability  $r_{\min}(\lambda)$  and the line  $r_{\max}(\lambda)$ , on which the locations of the two limit cycles merge. In the shaded region, where  $r_c > r_{\max}$ , no limit cycles are found. Red points mark the parameters used for the stroboscopic maps in figures 4 and 6 and the histograms in Fig 5, green points those for the histograms in Fig 7.

expansion of the real parts of these eigenvalues gives

$$\operatorname{Re}(s_B) = -r_c \frac{(1-\lambda)^4(1-10\lambda+\lambda^2)}{16(1-6\lambda+\lambda^2)} + O(r_c^3) \quad (38)$$

for the first pair, and

$$\operatorname{Re}(s_B) = -r_c \frac{(1-\lambda)^6}{16(1-6\lambda+\lambda^2)} + O(r_c^3) \quad (39)$$

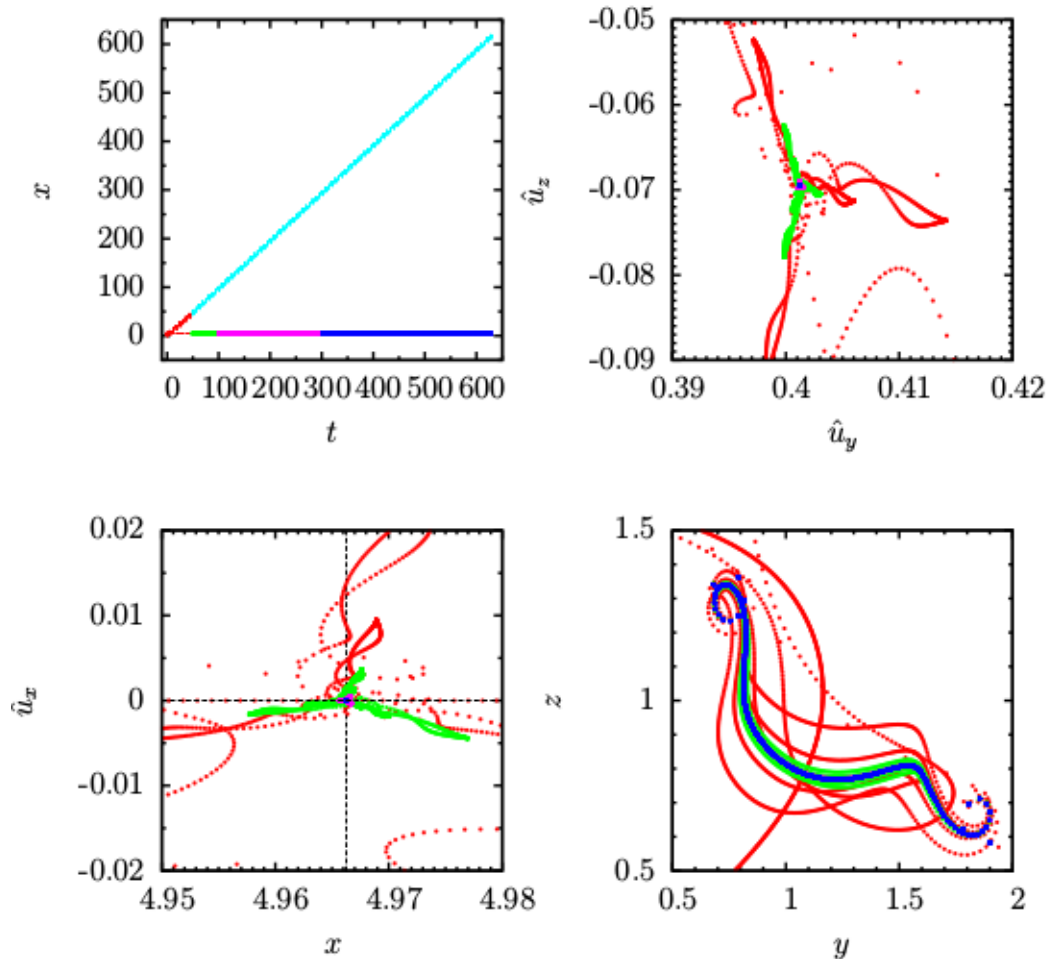
for the second. Thus, for sufficiently small  $r_c$ , the limit cycle is stable for  $\lambda < 5 - \sqrt{24} \approx 0.1$ , and unstable otherwise. For arbitrary  $r_c$ , an explicit expression for the eigenvalues in closed form is cumbersome, but easily found, using, for example, *Mathematica*.

The properties of the limit cycles are shown in figure 2 for three illustrative values of  $r_c$ . Note that the orbits at  $x = x_E$  (shown in red) are unstable for all values of  $\lambda$ , whereas there exists a range of  $\lambda$  in which the orbits at  $x = x_B$  (shown in blue) are stable. This is shown in more detail in the contour plot of figure 3. For each value of  $\lambda$ , limit cycles exist only for  $r_c < r_{\max}$ . For  $r_{\min} < r_c < r_{\max}$ , the cycles at  $x = x_B$  are stable, whereas for  $r_c < r_{\min}$ , they are unstable. Note, in particular, that for  $\lambda < 0.1$  the limit cycle at  $x_B$  is stable for all  $r_c$ , as suggested by the approximate solutions given in equations (38) and (39).

#### 4. Stroboscopic maps

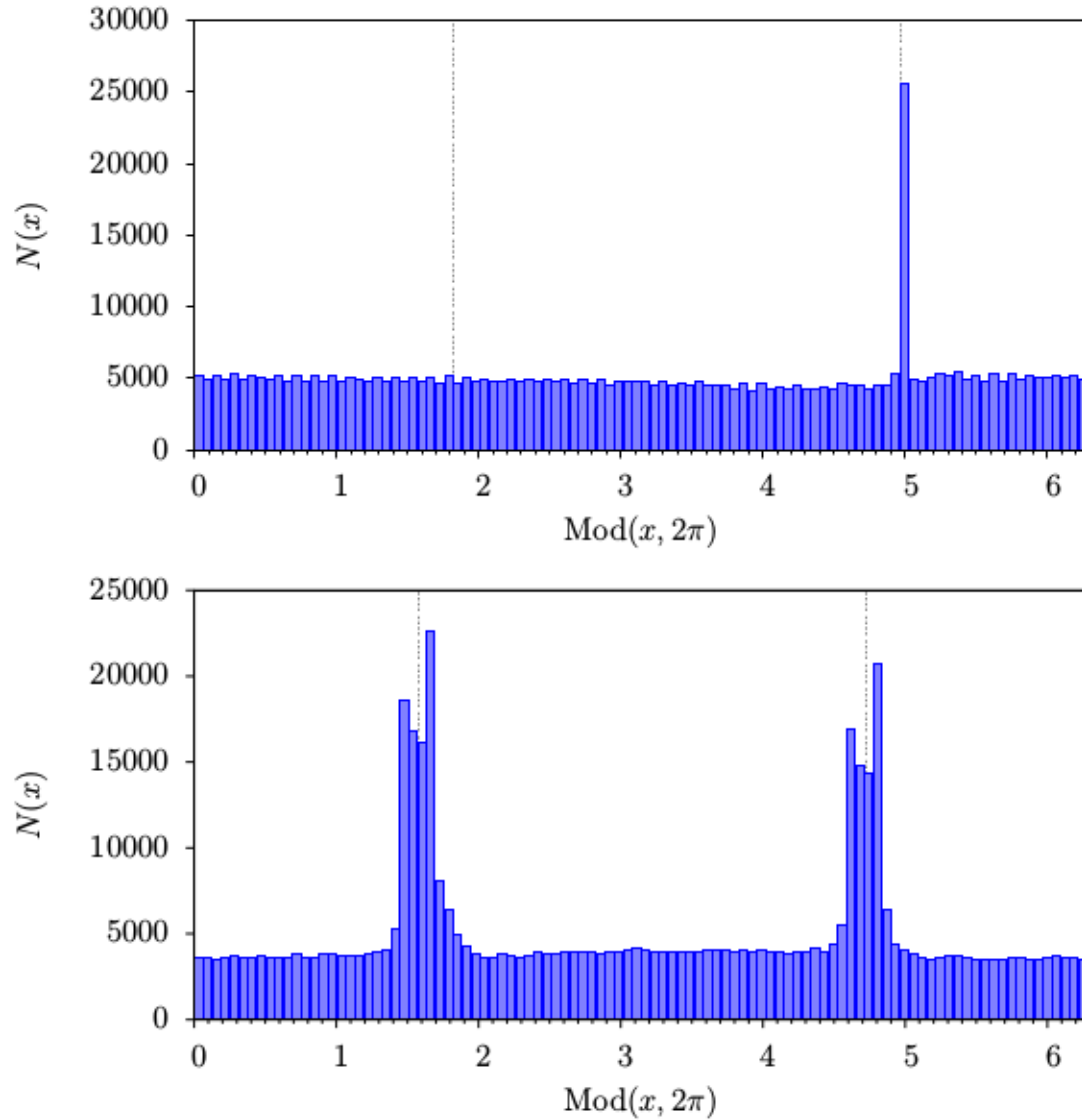
A linear stability analysis can give only a rough indication of the relevance of a limit cycle in a physical situation. For this reason, we have performed numerical integration of the driven dynamical system (11–14) and constructed stroboscopic maps giving the locations of the orbits in phase space at times  $\hat{t} = 2\pi n$ , where  $n$  is a positive integer. Results are presented for the choices of  $\lambda$  and  $r_c$  marked in figure 3 by red dots. For parameters corresponding to the green dots in this figure we present only histograms showing the cumulative number of trajectories at a given value of  $\operatorname{mod}(x, 2\pi)$ .

Figure 4 shows results for  $\lambda = 0.2$ ,  $r_c = 3$ , which lies in the stable region of Fig 3. Trajectories of 5000 positrons are integrated from  $t = 0$  to  $t = 200\pi$ , initiated at equally spaced points in  $x$  between 0 and  $2\pi$ , with  $\hat{u}_x = 0$ ,  $\hat{\gamma} = 1$  (i.e.,  $\gamma = a_0$ ) and values of  $\hat{P}_r$  and  $\Theta$  corresponding to  $\hat{u}_y = \hat{u}_z = 1/\sqrt{2}$ . Points depict the location in phase space at times  $t = 2n\pi$  for  $n = 0, 1, \dots, 200$ . The top left panel shows the  $t$ - $x$  plane, with various colour codes that serve to identify the corresponding points in the other three panels. For  $0 < t < 50$ , points are shown in red. After only a few wave periods, the trajectories separate into two groups: those that are picked up by the primary wave and acquire a high momentum in the positive  $x$ -direction (coloured light blue) and those that become trapped close to a limit cycle near the origin of the  $x$ -axis. The latter group is subdivided, as shown, according to the elapsed time. The remaining panels concentrate on the trapped particles. The top right panel plots the components of the four-momentum (normalized to  $a_0 mc$ ) in the transverse ( $y$ - $z$ ) plane. The trajectories converge rapidly to a point, indicating periodic motion. The bottom left panel shows



**Figure 4.** Stroboscopic plots of 5000 trajectories integrated for 100 wave periods using parameters  $\lambda = 0.2$ ,  $r_c = 3$  that permit a stable limit cycle according to figure 3. The upper left panel shows a clear separation into trapped and untrapped particles after a few wave periods. For  $t < 50$ , points are shown in red. For  $t > 50$ , points on untrapped trajectories are plotted in light-blue, whereas those on trapped trajectories are plotted in colours that change according to the elapsed time, as shown in the upper left panel. In the lower left panel, the  $x-\hat{u}_x$  plane is plotted, with the position of the stable limit cycle indicated by the intersection of the dashed lines. The right-hand panels show the phase space components transverse to the propagation direction.

a small part of the  $x-\hat{u}_x$  plane, close to the location of the limit cycle at  $x = x_B$  found in section 3, which is marked by the vertical dashed line. This panel illustrates rapid convergence to the limit cycle: for  $50 < t < 100$  (color-coded green), the trapped particles lie within  $\pm 0.04$  of the computed position of the limit cycle, and continue to converge even more tightly at later times. The lower right panel shows position in the transverse plane. Here the trajectories converge to a line rather than a point, indicating the presence of a slow drift of the orbits in this plane that is not strictly periodic at the fundamental frequency.



**Figure 5.** Histograms of the binned  $x$  coordinates. The upper panel shows the stable case corresponding to figure 4 ( $\lambda = 0.2$ ,  $r_c = 3$ ), and the lower panel the unstable case corresponding to figure 6 ( $\lambda = 0.4$ ,  $r_c = .5$ ). The locations of the limit cycles at  $x = x_B$  are indicated by the dashed lines.

The concentration of particles around the limit cycle is also clearly seen in the histogram presented in the upper panel of figure 5. Here, the  $x$  values measured at times  $2\pi n$  are mapped onto the interval  $[0, 2\pi]$  and accumulated in 100 bins. From the total of 5000 computed trajectories, this figure shows that approximately 250 are trapped at the location of a stable limit cycle.

For parameters  $\lambda = 0.4$ ,  $r_c = 0.5$ , which lies in the unstable region of figure 3, the stroboscopic plots are shown in Fig 6 and the corresponding histogram is the lower panel of figure 5. The trajectories no longer converge exactly onto the limit cycle, but, nevertheless, remain trapped in its immediate vicinity. The component of the

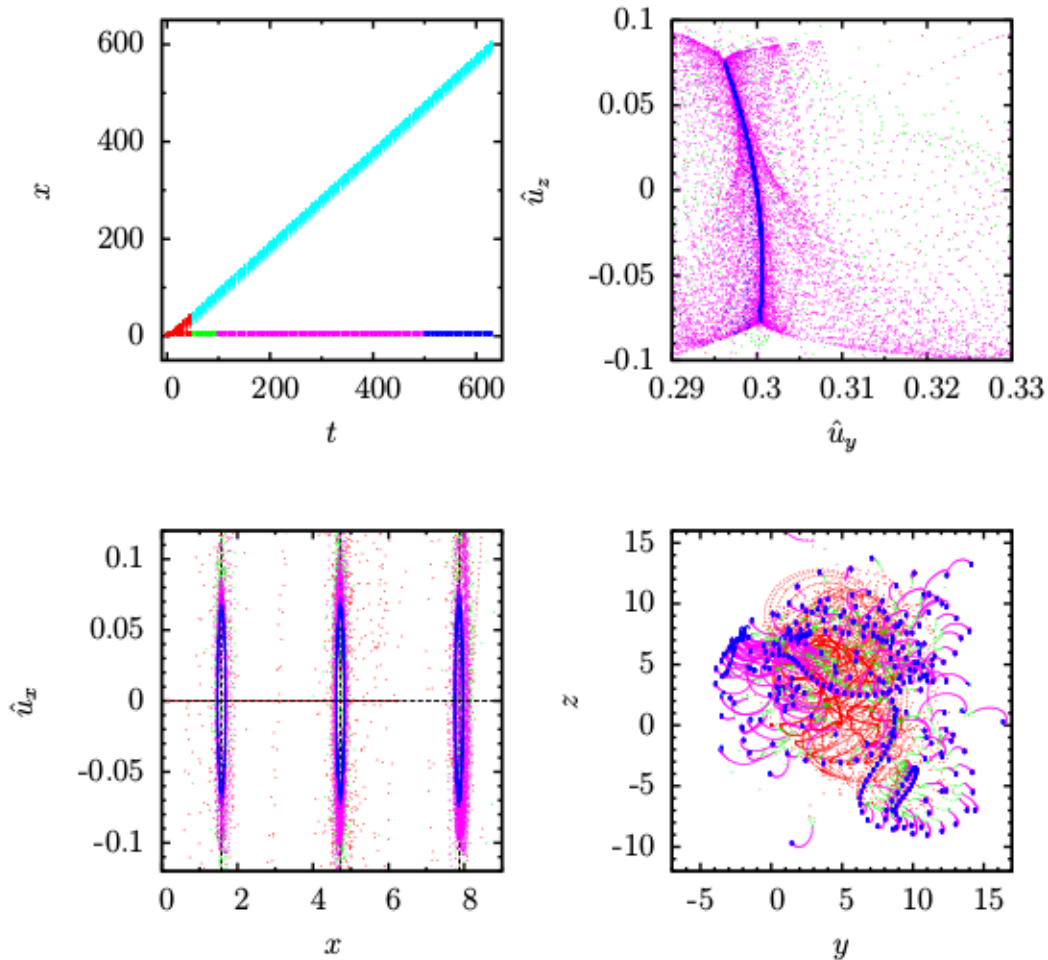


**Figure 6.** Stroboscopic plots of trajectories integrated for 100 wave periods for  $\lambda = 0.4$  and  $r_c = 0.5$  — values that do not permit a stable limit cycle according to figure 3. The unstable limit cycles at  $x = x_B$ ,  $\hat{u}_x = 0$  are located at the intersections of the dashed lines in the lower left panel.

particle momentum along the wave propagation direction oscillates with an amplitude of roughly  $0.05a_0mc$ , and the projection of the trajectory onto the transverse plane reveals a complex drifting pattern, superposed on almost circular motion. The lower panel of Fig 5 shows that particles are trapped in a range of  $x$  that is approximately 10% of one wavelength. Roughly 1500 of the 5000 trajectories are trapped — significantly more than in the linearly stable case.

Histograms of position are shown in Fig 7 for parameters corresponding to the green points in figure 3. As illustrated in the upper panel, strong trapping is a prominent feature wherever a limit cycle at  $x = x_B$  exists, independent of whether or not it is stable. For the chosen parameters ( $\lambda = 0.6$ ,  $r_c = 0.5$ ), approximately 1800 of the 5000 trajectories are confined close to the unstable limit cycle. However, as can be seen from

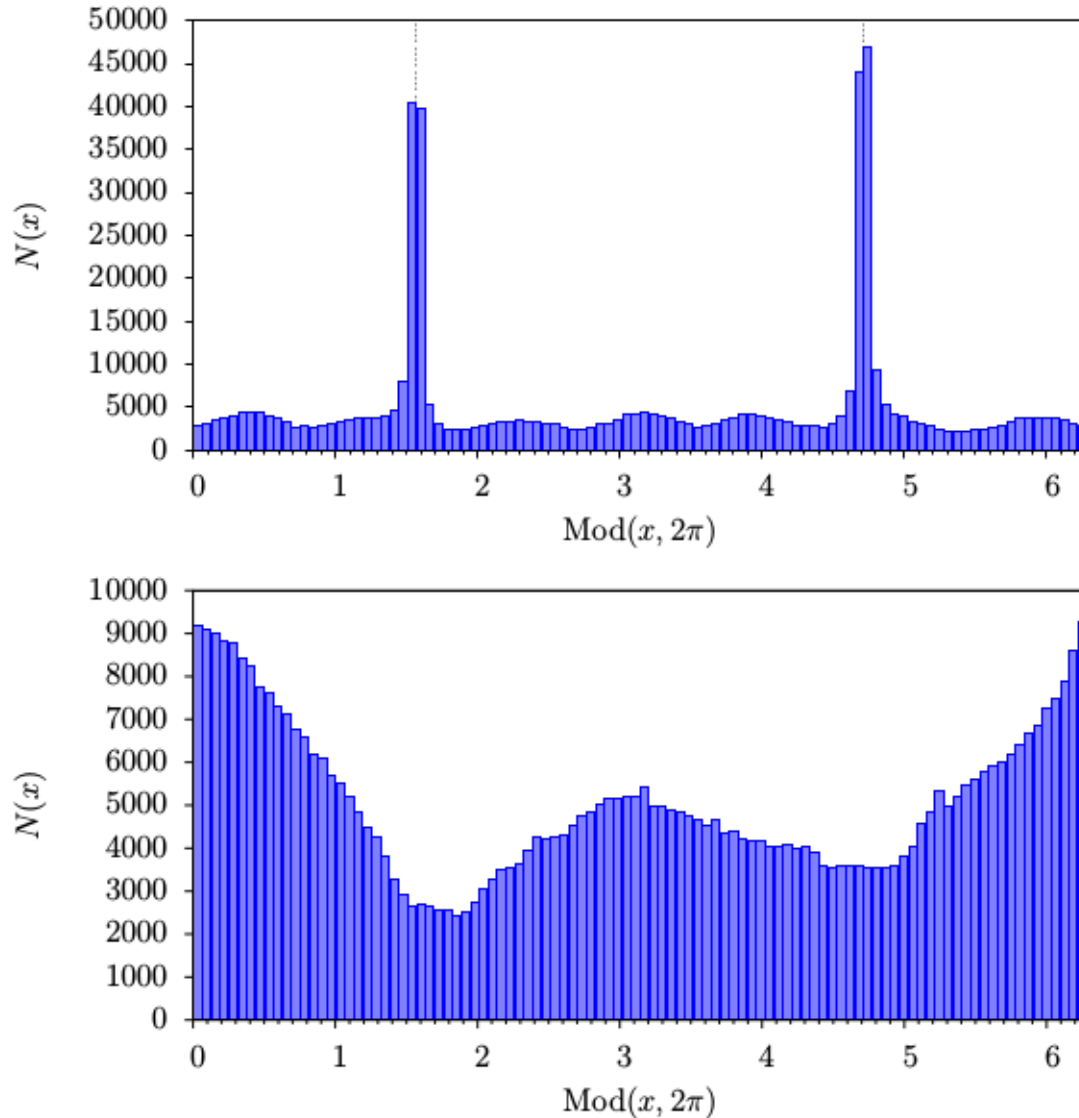


**Figure 7.** Histograms of the binned  $x$  coordinates for the parameters  $\lambda = 0.6$ ,  $r_c = 0.5$ , in the unstable region of figure 3 (upper panel) and for  $\lambda = 0.1$ ,  $r_c = 3$ , in the region of figure 3 in which no limit cycles are found (lower panel).

figure 2, the limit cycle in this case has values of  $\hat{\gamma}$  and  $\hat{\eta}$  that are well approximated by equations (28) and (29) and are, therefore, substantially smaller than those encountered for the same  $r_c$  in the stable range of  $\lambda$ . On the other hand, trapping is absent when no limit cycle can be found, as shown in the lower panel of figure 7 for  $\lambda = 0.1$  and  $r_c = 3$ . In this parameter regime, the radiation reaction force associated with the stronger wave (wave 1) is too strong to be balanced by the weaker wave and accelerates particles to high momentum in the positive  $x$  direction.

## 5. Discussion

In the absence of radiation reaction, the classical motion of a charged particle moving in a circularly polarized, monochromatic plane wave is a combination of periodic motion and a constant drift speed. Radiation reaction destroys this pattern, causing the particle to be swept along in the direction of propagation of the wave and accelerated to arbitrarily high energy. However, the results of the previous sections show that the presence of a weaker, counter-propagating, secondary wave can stabilize the motion. In the ZMF, in which the secondary wave has the same frequency as the primary, a substantial number of particles accumulate in a plane that is fixed in configuration space — they are *trapped* at precisely determined locations on the axis of propagation of the waves (at  $x = x_B$  in the notation of section 3) and execute almost circular motion in the plane transverse to this direction. On these orbits, the particle velocity is always parallel to the local magnetic field, as in the case of the self-consistent structures analyzed in [22].

For this to be possible, the secondary wave must have opposite helicity to that of the primary. Furthermore, its amplitude must exceed a certain threshold, which depends on the classical radiation reaction parameter  $r_c$ , and can be read off from figure 3. In terms of the intensity  $I_{24} \times 10^{24} \text{ W cm}^{-2}$  and wavelength  $\lambda_{\mu\text{m}}$   $\mu\text{m}$  of the primary wave,

$$r_c = 21 \times I_{24}^{3/2} \lambda_{\mu\text{m}}^2. \quad (40)$$

Immediately above the threshold, the limit cycle underlying the attractor is linearly stable, and particle orbits converge onto it asymptotically. Linear stability is lost at a point higher above threshold, but particles still accumulate very close to the limit cycle, performing chaotic motion on a strange attractor. As the intensity of the secondary wave approaches that of the primary, a larger fraction of the trajectories sampled in section 4 become trapped, and the growth rate of the linear instability weakens. Particles moving on this limit cycle have orbits that are well-approximated by equations (25)–(29), unless  $\lambda$  is very close to or below threshold. The corresponding values of the Lorentz factor and QED parameter  $\eta$  are

$$\gamma \approx 605 \times (1 - \lambda) I_{24}^{1/2} \lambda_{\mu\text{m}} \quad (41)$$

$$\eta = 0.89 \times (1 - \lambda)^2 I_{24} \lambda_{\mu\text{m}}. \quad (42)$$

Photons are radiated incoherently by particles moving on the attractor, and have a synchrotron-like spectrum, which peaks at the energy

$$E_\gamma = 0.65 \times r_c \hat{\gamma}^3 (mc^2 / \alpha_f) \quad (43)$$

$$\approx 120 \times (1 - \lambda)^3 I_{24}^{3/2} \lambda_{\mu\text{m}}^2 \text{ MeV}, \quad (44)$$

where  $\alpha_f$  is the fine-structure constant. Thus, although more trajectories are trapped for larger  $\lambda$ , this region results in lower values of  $\gamma$  and  $\eta$ , so that the optimal value for creating hard gamma-rays and/or observing QED effects lies close to the threshold.

As a potential application, consider a set-up similar to that adopted in [24], where relativistic, resonant phase-locking in a single, circularly polarized wave has been proposed as an attractive mechanism for the production of gamma-rays and relativistic electron beams. For a primary wave of intensity  $I_{24} = 0.08$  and  $\lambda_{\mu\text{m}} = 1$  one finds  $r_c = 0.5$ . Thus, introducing a counter-propagating circularly polarized pulse of opposite helicity, and with an intensity of roughly 16% of the primary wave would reproduce the conditions investigated in figure 6 and the upper panel of figure 7, leading to the emission of gamma-rays of energy roughly 2 MeV, highly collimated into a fan beam in the plane perpendicular to the direction of wave-propagation. For a primary wave with  $I_{24} = 0.2$  and  $\lambda_{\mu\text{m}} = 1$ , a secondary wave with 4% of this intensity produces an attractor on which  $\eta \approx 0.1$ , which lies within the range expected to lead to a non-linear pair cascade [25].

In addition to the limit cycle that underlies the attractor, another exists at  $x = x_E$ . In the limit of a standing wave ( $\lambda = 1$ ), this is the orbit studied by Bell & Kirk [25], who used it to analyze the possibility of generating a non-linear cascade of electron-positron pairs. On it, the values of  $\hat{\gamma}$  and  $\hat{\eta}$  are much larger than those found on the cycle at  $x = x_B$ . However, figure 2 shows that this orbit is linearly unstable, with a growth rate that is of the same order as the wave frequency, and substantially exceeds that of the unstable modes at  $x = x_B$ . Furthermore, the results of section 4 show no indication of the existence of an attractor related to this limit cycle, in agreement with subsequent work on cascades [20].

The lack of an attractor with a strong electric field in a circularly polarized standing wave has led to the suggestion that linear polarization might provide a more effective means of realizing non-linear pair cascades [19]. Attractors of the kind described above, in which the orbit lies in the plane transverse to the propagation vector, can be found in this case only if the polarization vectors of the two waves are precisely aligned, and the wave intensities are exactly equal. Standing waves in this configuration have been investigated in [16], where trapping was found not only on an attractor at the analogue of  $x = x_B$ , but also, for very high intensities, at the analogue of  $x = x_E$ . This phenomenon has no counterpart in the circularly polarized case discussed above, where the limit cycles at  $x_E$  are strongly unstable at all intensities. However, the limit cycle orbit in linear polarization is rectilinear. Consequently, the radiation mechanism — *linear acceleration emission* [26, 27] — differs significantly from synchrotron radiation, and equation (9) is not an adequate approximation to the radiation reaction force [28], which becomes a very sensitive function of the longitudinal momentum  $u_x$ . In addition to modifying the stability properties, this effect also leads to a relatively low value of the QED parameter  $\eta$ , making it more difficult for trapped particles to enter the regime of strong field QED.

The results presented above are subject to several limitations. Firstly, they are based on an analysis of the equations of motion in classical electrodynamics, assuming highly relativistic motion, and using an approximate formulation of the radiation reaction force due to [21]. This requires that the QED effects be minor, i.e.,  $\eta \ll 1$ .

For improved accuracy, the classical radiation reaction term can be modified by the function  $g(\eta)$  as described by [20]. This correction is straightforward to implement, but introduces an additional parameter, and does not produce any qualitative changes. For  $\eta > 0.1$ , the influence of *straggling* [29, 30, 31] becomes important, and the structure of the attractors is expected to change [19], although it is unlikely that they disappear entirely. Secondly, a plane-wave approximation is used. The lower right panels in figures 4 and 6 show that the attractors drift around in the transverse plane over a region with a typical extension of a few wavelengths. In a realistic situation, for example, a tightly focused pulse, transverse structure in the fields might limit the time for which trajectories remain trapped. Thirdly, the waves are assumed to be circularly polarized and monochromatic. Relaxing this assumption makes an analytical treatment difficult, and it is not clear whether or not the attractors described above are generic features. Fortunately, none of these limitations applies to numerical simulations in which strong-field QED effects have been implemented (e.g., [14]), so that their importance under more realistic condition can readily be checked.

## 6. Conclusions

The class of electron limit cycles identified in section 3 underlies the phenomenon of radiative trapping on attractors. A numerical study (section 4) shows that they have a simple structure where the corresponding limit cycle is stable, but that they also extend into the unstable region, where they become chaotic. This enables the electron dynamics in counter-propagating, circularly polarized laser pulses to be controlled by adjusting the relative intensity  $\lambda$  of the pulses, according to figure 3. In intense optical pulses with  $I \sim 10^{23} \text{ W cm}^{-2}$ , the radiation reaction parameter  $r_c \sim 1$ , and the regime of strong-field QED is best realized using a secondary probe beam with an intensity equal to a few percent of the primary.

These results are based on the equations of motion of classical electrodynamics, using a relativistic approximation to the radiation reaction term as formulated by Landau & Lifshitz [21]. To test their applicability to realistic, 10 PW pulses, a full numerical treatment including quantum effects is required.

## Acknowledgments

I thank Antonino di Piazza, Tony Bell and Chris Ridgers for helpful discussions.

## References

- [1] Extreme Light Infrastructure. <http://www.eli-beams.eu>. Accessed: 2016-03-25.
- [2] Exawatt Centre for Extreme Light Studies. <http://www.xcels.iapras.ru>. Accessed: 2016-03-25.
- [3] European High Power Laser Energy Research Facility. <http://www.hiper-laser.org>. Accessed: 2016-03-25.

- [4] A. Di Piazza, C. Müller, K. Z. Hatsagortsyan, and C. H. Keitel. Extremely high-intensity laser interactions with fundamental quantum systems. *Reviews of Modern Physics*, 84:1177–1228, July 2012.
- [5] A. di Piazza. Exact solution of the Landau-Lifshitz equation. *Lett. Math. Phys.*, 83:305–313, 2008.
- [6] J. T. Mendonca and F. Doveil. Stochasticity in plasmas with electromagnetic waves. *Journal of Plasma Physics*, 28:485–493, December 1982.
- [7] D. Bauer, P. Mulser, and W.-H. Steeb. Relativistic ponderomotive force, Uphill acceleration, and transition to chaos. *Physical Review Letters*, 75:4622–4625, December 1995.
- [8] G. Lehmann and K. H. Spatschek. Phase-space contraction and attractors for ultrarelativistic electrons. *Phys. Rev. E*, 85(5):056412, May 2012.
- [9] A. Zhidkov, J. Koga, A. Sasaki, and M. Uesaka. Radiation Damping Effects on the Interaction of Ultraintense Laser Pulses with an Overdense Plasma. *Physical Review Letters*, 88(18):185002, May 2002.
- [10] N. Naumova, T. Schlegel, V.T. Tikhonchuk, C. Lobaune, I.V. Sokolov, and G. Mourou. Ponderomotive ion acceleration in dense plasmas at super-high laser intensities. *The European Physical Journal D*, 55(2):393–398, 2009.
- [11] M. Tamburini, F. Pegoraro, A. Di Piazza, C.H. Keitel, and A. Macchi. Radiation reaction effects on radiation pressure acceleration. *New Journal of Physics*, 12(12):123005, 2010.
- [12] M. Chen, A. Pukhov, T-P. Yu, and Z-M. Sheng. Radiation reaction effects on ion acceleration in laser foil interaction. *Plasma Physics and Controlled Fusion*, 53(1):014004, 2011.
- [13] T. Nakamura, J. Koga, T. Esirkepov, M. Kando, G. Korn, and S.V. Bulanov. High-power gamma-ray flash generation in ultraintense laser-plasma interactions. *Physical Review Letters*, 108(19), 2012.
- [14] C. P. Ridgers, J. G. Kirk, R. Duclous, T. G. Blackburn, C. S. Brady, K. Bennett, T. D. Arber, and A. R. Bell. Modelling gamma-ray photon emission and pair production in high-intensity laser-matter interactions. *Journal of Computational Physics*, 260:273–285, March 2014.
- [15] S. V. Bulanov, T. Z. Esirkepov, M. Kando, J. Koga, K. Kondo, and G. Korn. On the problems of relativistic laboratory astrophysics and fundamental physics with super powerful lasers. *Plasma Physics Reports*, 41:1–51, January 2015.
- [16] A. Gonoskov, A. Bashinov, I. Gonoskov, C. Harvey, A. Ilderton, A. Kim, M. Marklund, G. Mourou, and A. Sergeev. Anomalous Radiative Trapping in Laser Fields of Extreme Intensity. *Physical Review Letters*, 113(1):014801, July 2014.
- [17] L. L. Ji, A. Pukhov, I. Y. Kostyukov, B. F. Shen, and K. Akli. Radiation-Reaction Trapping of Electrons in Extreme Laser Fields. *Physical Review Letters*, 112(14):145003, April 2014.
- [18] T. Z. Esirkepov, S. S. Bulanov, J. K. Koga, M. Kando, K. Kondo, N. N. Rosanov, G. Korn, and S. V. Bulanov. Attractors and chaos of electron dynamics in electromagnetic standing waves. *Physics Letters A*, 379:2044–2054, September 2015.
- [19] M. Jirka, O. Klimo, S. V. Bulanov, T. Zh. Esirkepov, E. Gelfer, S. S. Bulanov, S. Weber, and G. Korn. Electron dynamics and  $\gamma$  and  $e^-e^+$  production by colliding laser pulses. *Phys. Rev. E*, 93:023207, Feb 2016.
- [20] J. G. Kirk, A. R. Bell, and I. Arka. Pair production in counter-propagating laser beams. *Plasma Physics and Controlled Fusion*, 51(8):085008, August 2009.
- [21] L. D. Landau and E. M. Lifshitz. *The Classical Theory of Fields*. Course of theoretical physics - Pergamon International Library of Science, Technology, Engineering and Social Studies, Oxford: Pergamon Press, 1975, 4th rev.engl.ed., 1975.
- [22] J. G. Kirk, A. R. Bell, and C. P. Ridgers. Pair plasma cushions in the hole-boring scenario. *Plasma Physics and Controlled Fusion*, 55(9):095016, September 2013.
- [23] J. E. Gunn and J. P. Ostriker. On the Motion and Radiation of Charged Particles in Strong Electromagnetic Waves. I. Motion in Plane and Spherical Waves. *Astrophysical J.*, 165:523, May 1971.

- [24] B. Liu, R. H. Hu, H. Y. Wang, D. Wu, J. Liu, C. E. Chen, J. Meyer-ter-Vehn, X. Q. Yan, and X. T. He. Quasimonoeenergetic electron beam and brilliant gamma-ray radiation generated from near critical density plasma due to relativistic resonant phase locking. *Physics of Plasmas*, 22(8):080704, August 2015.
- [25] A. R. Bell and J. G. Kirk. Possibility of Prolific Pair Production with High-Power Lasers. *Physical Review Letters*, 101(20):200403–+, November 2008.
- [26] D. B. Melrose, M. Z. Rafat, and Q. Luo. Linear Acceleration Emission. I. Motion in a Large-Amplitude Electrostatic Wave. *Astrophysical J.*, 698:115–123, June 2009.
- [27] B. Reville and J. G. Kirk. Linear Acceleration Emission in Pulsar Magnetospheres. *Astrophysical J.*, 715:186–193, May 2010.
- [28] S. V. Bulanov, T. Z. Esirkepov, M. Kando, J. K. Koga, and S. S. Bulanov. Lorentz-Abraham-Dirac versus Landau-Lifshitz radiation friction force in the ultrarelativistic electron interaction with electromagnetic wave (exact solutions). *Phys. Rev. E*, 84(5):056605, November 2011.
- [29] R. Duclous, J. G. Kirk, and A. R. Bell. Monte Carlo calculations of pair production in high-intensity laser-plasma interactions. *Plasma Physics and Controlled Fusion*, 53(1):015009, January 2011.
- [30] N. Neitz and A. Di Piazza. Stochasticity Effects in Quantum Radiation Reaction. *Physical Review Letters*, 111(5):054802, August 2013.
- [31] T. G. Blackburn, C. P. Ridgers, J. G. Kirk, and A. R. Bell. Quantum Radiation Reaction in Laser-Electron-Beam Collisions. *Physical Review Letters*, 112(1):015001, January 2014.